Superlattice Effect for Enhanced Fracture Toughness of Hard Coatings

Diploma Thesis

by

Rainer Hahn

Christian Doppler Laboratory for Application Oriented Coating Development

at the Institue of Materials Science and Technology,

Technische Universität Wien

Wien, June 2016

This work was supported by Plansee Composite Materials GmbH and
Oerlikon Balzers, Oerlikan Surface Solutions AG, in the framework of the
Christian Doppler Laboratory for Application Oriented Coating Development.

Affidavit:
I declare in lieu of oath, that I wrote this thesis and performed the associated research myself, using only literature cited in this volume.

Date *Signature*

Acknowledgements

First of all I want to thank **Prof. Paul Heinz Mayrhofer** for giving me the opportunity to write this thesis through the Christian Doppler Laboratory for Application Oriented Coating Development. As my supervisor, he always supported and guided me not only the last months, but since I started working as a student worker in his thin film group.

I would like express my deep gratitude to my thesis adviser **Dr. Matthias Bartosik** for all the time he found for guiding me, for the great help and his constant support during the whole research work. No matter how often I needed advice or wanted to discuss some findings, he always had the patience and the knowledge to help.

Furthermore, I am also very grateful to all my colleagues within the **Thin Film Group** for further assistance concerning experiments and the great time I had during working on this thesis.

I want to thank my **family and friends** for all their support during the duration of my whole studies. Especially, I want to thank **Sabine**, for being always behind me and giving me the mental strength and energy to achieve my goals.

Contents

Abstract

Abstract

Protective hard coatings applied on cutting or milling tools operate under severe mechanical loads and harsh environments. They play a crucial role in industrial engineering components prolonging their lifetime and enhancing their properties. Ideally, the coatings should be both strong enough to withstand applied loads and tough enough to prevent premature failure as a result of crack initiation and propagation.

In the 1970s J.S. Koehler theoretically predicted for solid matter that, by reason of the inability of Frank-Read sources to operate when a system possesses a sufficient small (nano-) layer structure, the shearing resistance and therefore the mechanical properties might be improved significantly. These so called superlattices structures (SLS), composed of two alternating coherent ceramic materials with the thickness of the layers in the nanometer range, are nowadays a well-accepted approach for designing hard coatings. So far, the multilayered systems with a bilayer period of some nanometer have been extensively investigated in terms of hardness, exceeding the value of their single layered components by some hundred percent. However the influence of superlattice structures on the fracture toughness of superlattice thin films has yet to be reported.

In the present diploma thesis, the effect of the bilayer period on the fracture toughness of ceramic TiN/CrN superlattice structures was analyzed. All coatings were deposited in a plasma-assisted reactive magnetron sputtering process using a computer controlled shutter system to obtain alternating, equal thick layers of TiN and CrN. X-Ray diffraction analysis was used to verify the formation of an exclusively cubic thin film and to evaluate the interface-quality of the superlattice system. The basic mechanical properties, indentation hardness and the young's modulus, of these hard coatings were investigated by performing nanoindentation experiments. Thereby the pronounced superlattice effect on the indentation hardness was found for TiN/CrN superlattice systems whilst the youngs modulus shows no dependence of the bilayer period.

The fracture toughness was determined by performing *in-situ* micromechanical cantilever bending tests on freestanding TiN/CrN thin films. It was found that, while the fracture toughness of the multilayer systems is close to that of the more brittle component (CrN) for large bilayer periods ($\Lambda > 10\,\mathrm{nm}$), it increases with decreasing bilayer period reaching a maximum at $\Lambda \sim 6\,\mathrm{nm}$. For very thin layers the K_{IC} value drops below that of the weaker film component (CrN). Interestingly, the findings clearly show a coincidence between the hardness peak and the fracture toughness peak suggesting the same size dependent mechanisms to be operative.

The results indicate a possible new strategy for alleviating the inherent brittleness of a hard coating while retaining its favorable properties, predicting a further improvement of recently developed hard coatings by a feasible deposition of a superlattice system. Furthermore it is anticipated that the size effect of both, the fracture toughness and the indentation hardness, could be significantly increased by optimizing the deposition parameters.

Kurzfassung

Schützende Hartstoffschichten auf Schneidwerkzeugen werden im Einsatz hohen mechanischen Belastungen und extremen Umwelteinflüssen ausgesetzt. Sie spielen hierbei eine entscheidende Rolle für Maschinenelemente da sie sowohl deren Lebensdauer verlängern als auch deren Eigenschaften verbessern. Idealerweise sollte eine solche Beschichtung hart genug sein um den auftretenden Kräften Stand zu halten als auch zäh genug um ein vorzeitiges Versagen durch Rissinitiierung und Rissausbreitung zu verhindern.

In den 1970er Jahren sagte J.S. Koehler voraus, dass feste Materie, bei ausreichend dünnen Einzelschichten, aufgrund der unterbundenen Versetzungsgenerierung durch Frank Read Quellen, einen außerordentlich hohen Scherwiderstand und somit exzellente mechanische Eigenschaften besitzt. Diese sogenannten Superlattice Strukturen (SLS), bestehend aus zwei alternierenden, nur wenigen Nanometer dicken, keramischen Materialien und sind mittlerweile eine weit verbreitete Herangehensweise um eine Hartstoffschicht mit herausragender Härte zu entwerfen. Bisher wurden diese SLS seitens der Materialforschung intensiv untersucht und es wurde von Eindringhärten berichtet, die den herkömmlichen Wert der Einzellagen um ein Vielfaches übersteigen. Allerdings gibt es bis heute keine quantitativen Aussagen über den Einfluss einer Superlattice Struktur auf die Bruchzähigkeit dieser Hartstoffschichten.

In dieser Diplomarbeit wurde die Auswirkung der Dicke der Einzellagen auf die Bruchzähigkeit von TiN/CrN Superlattice Strukturen untersucht. Alle Hartstoffschichten in dieser Arbeit wurden mittels eines Plasma-unterstütztem reaktivem Magnetron Sputtering Prozesses abgeschieden. Dabei wurde ein computergesteuertes Shutter System verwendet um al-

ternierende TiN und CrN Lagen (mit gleicher Dicke) herzustellen. Mittels Röntgendiffraktometrie wurde nachgewiesen, dass eine ausschließlich kubische Struktur in der Schicht vorherrscht, und dass die Übergänge zwischen den beiden Einzelschichten von guter Qualität (möglichst dünn) sind. Die grundlegenden mechanischen Eigenschaften, Härte und E-Modul, wurden mittels Nanoindentation ermittelt. Hierbei zeigte sich der vorhergesagte Superlattice-Effekt auf die Eindringhärte, der E-Modul wies keine Abhängigkeit von den Einzellagendicken auf.

Die Ermittlung der Bruchzähigkeit (K_{IC}) erfolgte durch mikromechanische *in-situ* Versuche bei denen ein freitragender Balken der zu untersuchenden Schicht durch eine abgerundete Diamantspitze bis zum Versagen belastet wurde. Es zeigte sich, dass bei größeren Einzellagendicken $> 10\,\text{nm}$ der Wert der Bruchzähigkeit in etwa dem der Einzelschicht (CrN) entspricht, jedoch bei kleiner werdenden Einzellagendicken steigt und sein Maximum bei ca. 3 nm erreicht. Für sehr dünne Lagen fällt der K_{IC} Wert unter dem von CrN. Das Maximum der Bruchzähigkeit sowie der Härte werden bei annähernd identen Einzellagendicken von TiN und CrN erreicht. Dies lässt darauf schließen, dass ähnliche größenabhängige Mechanismen vorliegen.

Diese Erkenntnis könnte einen möglichen Weg für die Überwindung der intrinsischen Sprödigkeit bei gleichzeitiger Beibehaltung von gewünschten Eigenschaften einer Hartstoffschicht darstellen. Es wäre somit möglich, kürzlich entwickelte Verschleißschutzschichten in Kombination mit anderen Hartstoffschichten durch Herstellung einer Superlattice Struktur weiter zu verbessern. Des Weiteren wird angenommen, dass der größenabhängige Effekt durch Optimierung der Wachstumsbedingungen während des Beschichtungsprozesses weiter gesteigert werden kann.

Chapter 1

Introduction

The metal cutting industry experienced substantial changes in last decades. In prior years the development of high speed steels fundamentally changed the way of forming metals. In the 1920s, investigations on cemented carbides as possible cutting and metal forming tool materials and their subsequent application improved the efficiency and fields of application for these tools. With the development of stronger materials, requiring higher cutting- and forming-forces and -temperatures, these tooling materials did not meet all requirements of the industry anymore and hence the path for modern surface engineering was paved [1].

There are different ways to create a surface which provides enhanced properties. A common and well established technique is depositing a protective layer by Physical Vapor Deposition (PVD). This technology allows the creation of a variety of metallic and ceramic coatings, even in metastable states, by evaporation of atoms from a target done for example by ion-bombardment, transportation and subsequent (reactive-) condensation on a substrate. Especially transition metal nitrides (TMN), such as CrN and TiN, are widely used in various industrial applications improving the properties and prolonging the lifetime of engineering components. Newer industrially used coating systems are for example $Ti_{1-x}Al_xN$, $Cr_{1-x}Al_xN$ and $Ti_{1-x}Si_xN$ [2].

Particularly interesting for metal cutting and forming applications are the mechanical and chemical properties of a coating. Because of the applied loads in combination with the harsh environment these tools operate, a coating needs to be resistant against wear, oxidation, and thermal decomposition. Therefore, for example, a lowering of the coefficient of friction, an increase of the hardness and the enhancement of the chemical inertness of these coatings are current issues of several research and development institutions [1].

For instance, a generally accepted approach for increasing the wear resistance is enhancing the hardness H of such a coating by depositing superlattice structures. These structures consist of alternating layers of coherent materials with a periodicity in the nanometer range,

exceeding the hardness of their single-layered constituents up to some hundred percent [3]. However, another crucial factor for preserving the integrity of a coating is, beside the former mentioned properties, the fracture toughness K_{IC}. A review article by Zhang *et al.* [4] shows several strategies for enhancing the fracture toughness of thin films, namely for example by incorporating a ductile phase or toughening through a nanograin structure. The influence of a superlattice structure on the fracture toughness is yet to be investigated. Consequently the goal of this work was to analyze and quantify a possible effect of the bilayer period (defined as the thickness of two consecutive single layers) on the fracture toughness and to compare this potential influence with the well-known superlattice induced hardening effect.

The TiN/CrN superlattice system was used as a model system due to its constituents identical crystal structure (face-centered cubic (B1)) [5, 6] and their different shear moduli promoting coherent film growth and the desired superlattice effect, respectively. The deposition of these coatings are often done with a sputtering system equipped with either a computer controlled shutter system or by alternate moving of the substrate holder to certain positions in front of the respective cathode. In principle, both techniques assure sharp interfaces between the single layers.

The measuring of the fracture toughness of a thin film is not standardized so far as in case of bulk materials. Due to this fact there is a variety of existing methods developed by several scientists [7, 8]. A precise and reliable method for quantifying the fracture toughness is in-situ micromechanical testing of Focused Ion Beam (FIB)-machined single cantilevers. These cantilevers are pre-notched and loaded in a way to ensure mode I stress conditions to obtain K_{IC} values [9].

Chapter 2

Theoretical Framework

The following chapter will provide some information of the coating process, the film growth, an overview of hard coatings, especially TiN and CrN, and a more detailed view on superlattice coatings and the TiN/CrN superlattice system.

2.1 Deposition and growth

There are several techniques existing for depositing a hard coating on an appropriate substrate, the most common for coating engineering components are: Thermally activated chemical vapor deposition (CVD), plasma assisted physical vapor deposition (PVD), and plasma assisted chemical vapor deposition (PACVD) [10]. The deposition of thin films by physical vapor deposition is generally characterized by following 3 steps:

- Vaporization of a target material (cathode)
- Transportation of the gaseous matter to the substrate
- (Reactive) condensation on the substrate.

The vaporization of the target can be accomplished by several methods, spanning from the most common and industrially used variants, sputtering and arc evaporation, to more infrequent and mostly for scientific purposes used techniques like electron beam evaporation, molecular beam epitaxy, or pulsed laser deposition. The technique used in this work was reactive unbalanced dc magnetron sputtering [10].

During magnetron sputtering (Fig. 2.1) a flux of sputtered atoms are deposited on substrates. The substrates are typically heated and placed perpendicular to the flux direction. Sputtered atoms are produced by plasma-ions hitting a target material which is biased by

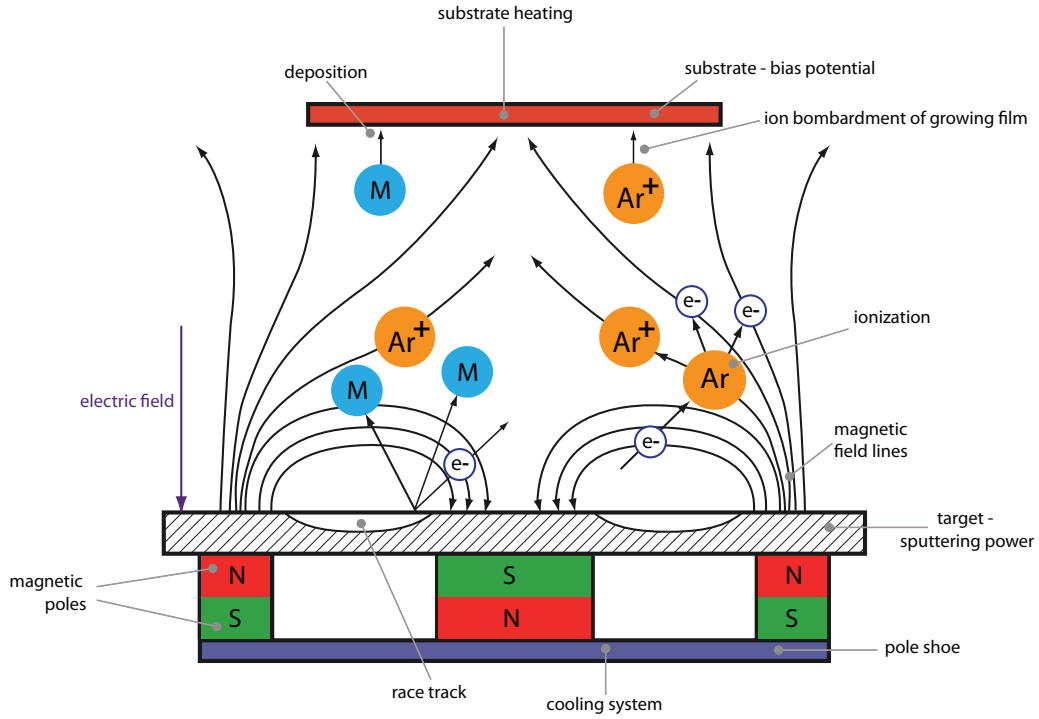

Figure 2.1: Unbalanced magnetron sputtering (UBM) process with stronger outer magnets [11].

the application of voltage (in this case a direct current voltage thus dc magnetron sputtering). For extended plasma torches towards the substrate, higher ionization of the plasma and higher depositing rate, an unbalanced magnetron (stronger permanent magnets on the outer side of the planar magnetron) is advantageous by reason of non-closing magnetic field lines. Reactive sputtering signifies a chemical reaction between the sputtered atoms and the process gas. Thus, instead of depositing a pure target material on the substrates, a chemical compound is deposited. Furthermore, in many industrial applications, a negative voltage applied on the substrates (bias-voltage) is used to create a denser coating by ion bombardment and consequential removal of atoms from the surface resulting in re-nucleation of the adatoms [10, 11].

All of the latter mentioned, and other parameters like gas pressure and the target-to-substrate-distance, can influence the film formation and characteristics [11]. The film formation generally depends on various atomistic parameters, for example the diffusion coefficient or the free surface energy, by reason of constant interactions between the atoms of the substrate and those of the thin film (those bound inside the thin film, as well as adatoms on the surface of the growing film). Depending on these material characteristics, three primary models were found that describe the film formation: Volmer-Weber (island formation), Frank-van-der-Merwe (layered-growth) and Stranski-Krastanov (combined growth), shown in Fig. 2.2 [12].

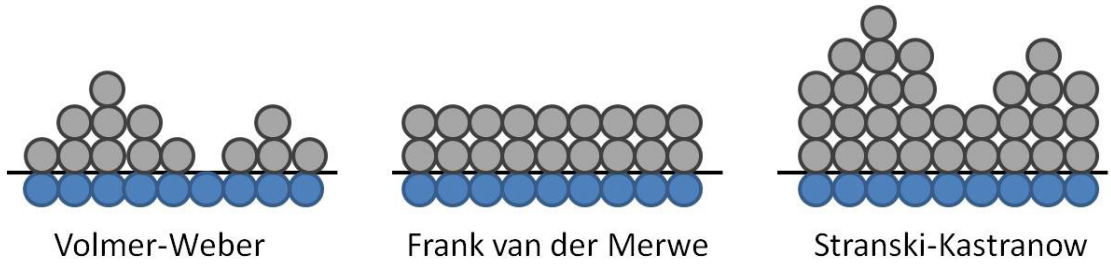

Figure 2.2: Growth mechanisms [12].

Of course these atomic interactions and hence the material characteristics can be modified by varying deposition parameters leading to a variety of different microstructures and consequently to different material properties. These relationships are well summarized in so called structure zone models (SZM). The influence of the homologous deposition temperature and the normalized energy used for the deposition process is for example given by the adapted structure zone model by Anders [13] shown in Fig. 2.3. More detailed information on these (mutual) influences can be found in literature [11].

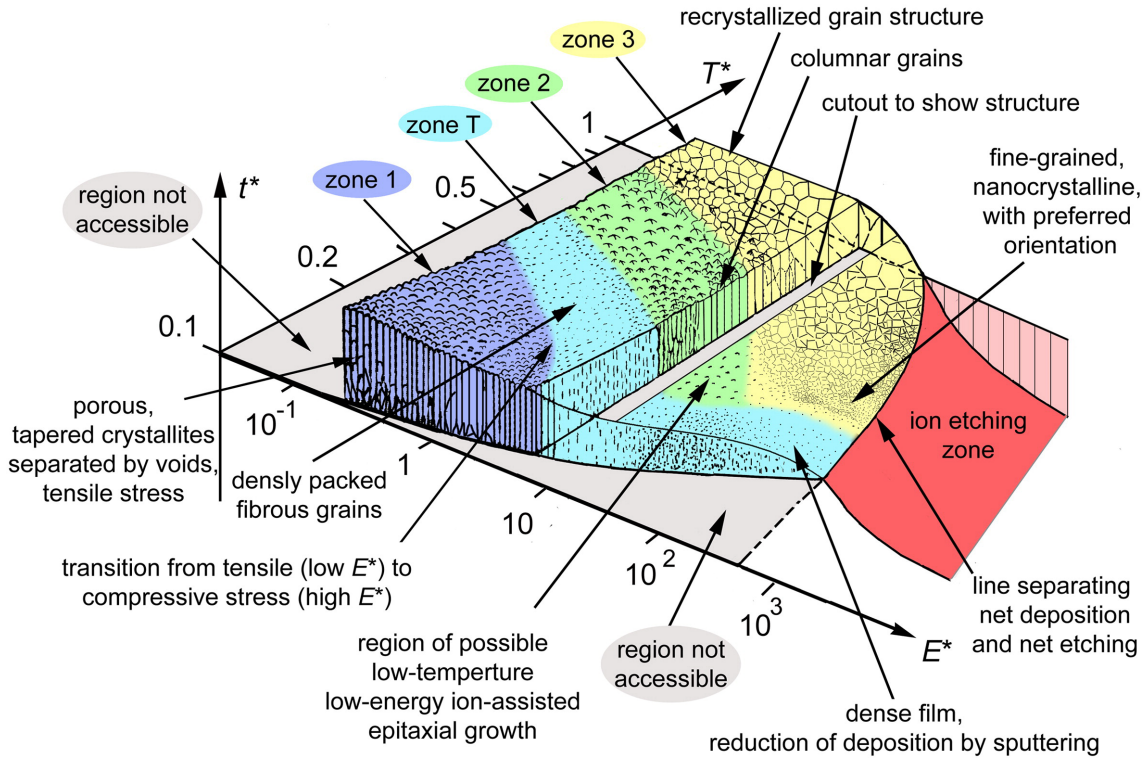

Figure 2.3: Adapted structure zone model by Anders [13].

2.2 Hard ceramic coatings

As mentioned in the introduction, hard coatings are used to protect engineering components such as molds and cutting tools from harsh environments and severe loads. Thus there is a need for strong chemical bonds in order to fulfill these requirements. One can distinguish these coatings by the type and proportion of chemical bonds (metallic, covalent and ionic) as shown in Fig. 2.4.

In the last decades borides, carbides, nitrides and oxides were developed and successfully applied in several industrial applications. Especially transition metal nitrides (TMN) possess attractive properties like high hardness, corrosion resistance, wear resistance, thermal stability and oxidation resistance. Similar to bulk materials, these properties can be modified by changing the microstructure, which can be done, as mentioned before, by adjusting deposition parameter or by alloying certain elements [11]. Advancements were made, for example, with partially substituting Ti or Cr by other elements, such as Al for enhanced mechanical properties and oxidation resistance in $Ti_{1-x}Al_xN$ or $Cr_{1-x}Al_xN$ [15, 16]. Further improvements can be achieved for example by depositing multilayer structures or by alloying elements with a high affinity to Oxygen like Yttrium to obtain a reactive-element effect (REE) to improve the oxidation resistance of the coating [17].

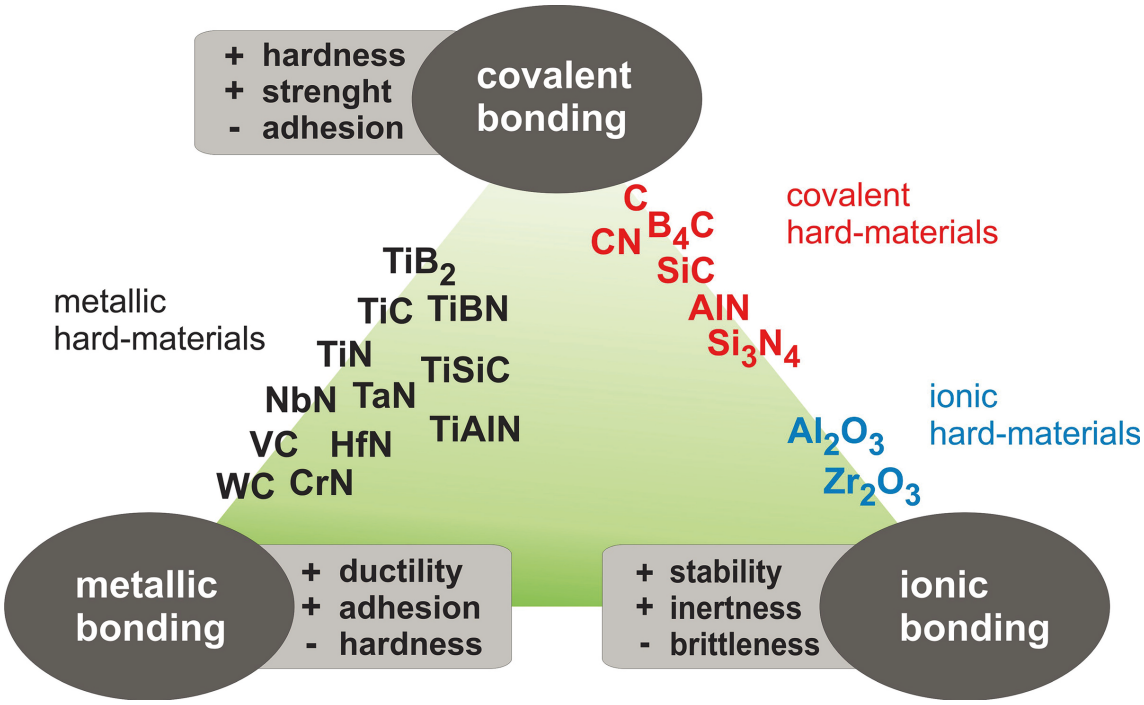

Figure 2.4: Classification of hard ceramic coating by their bonding character including a rough specification of their properties [14].

2.3 TiN coatings

As shown in Fig. 2.5, Titanium and Nitrogen form the face-centered cubic (rock salt type B1) TiN phase. It is an interstitial compound, often called Hagg-phase, and has a lattice parameter of $a_c = 4.241\,\text{Å}$. In this structure the Nitrogen is placed in the octahedron gap of the metallic Titanium-lattice, thus the chemical bonding of TiN is approximately half covalent and half metallic. Pure stoichiometric TiN has a gold color, as seen in many industrial applications. This phase is stable in a relatively wide range of different Nitrogen contents from room-temperatures to its melting point. When deposited with a higher Nitrogen percentage (in the Ar/N_2 gas mixture) than needed for the stoichiometric TiN, imperfections will develop due to the limited solubility of Nitrogen in TiN. Hence, the coating will appear in a more bronze to red color instead of the gold color for the stoichiometric TiN, reflecting those imperfections [6, 18]. Titanium Nitride hard coatings have a hardness of $\sim 27\,\text{GPa}$, an indentation modulus of about 380 GPa and their coefficient of friction (COF) is approximately 0.4. The chemical inertness of these coatings and the good mechanical properties ensure the role of TiN as a designated representative for ceramic hard coatings, industrially used since the 1960s [19].

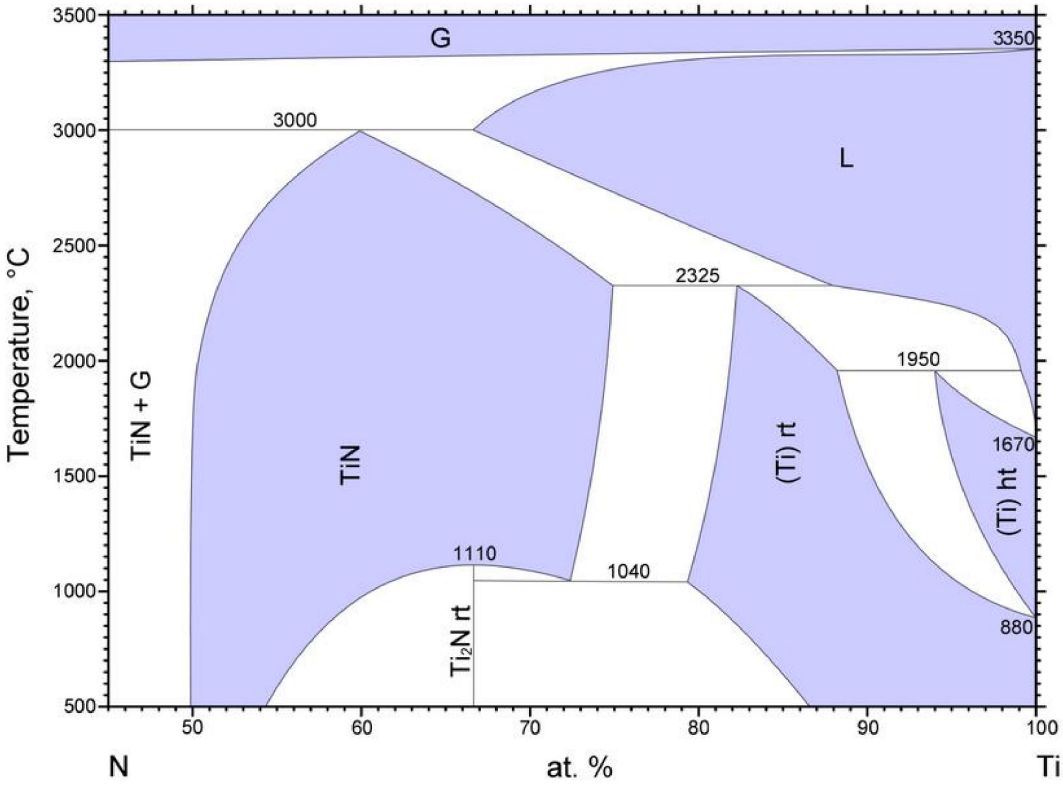

Figure 2.5: Calculated binary phase diagram N-Ti [20].

2.4 CrN coatings

Chromium nitride is, like TiN, an intermetallic compound of Chromium and Nitrogen. There are two different modifications of interest of this compound existing at room temperature: the cubic CrN phase and the hexagonal Cr_2N phase, see Fig. 2.6. In the main focus of this work is the CrN phase because of its cubic crystal structure and the consequential coherent film growth on cubic TiN. The cubic phase (B1 rock salt structure) has a lattice parameter of $a_c = 4.140\,\text{Å}$. The chemical bonding of CrN is characterized, compared with TiN, by a more metallic than covalent characteristic with a small amount of ionic bonding character (see Fig. 2.4). The compositional range where CrN is stable is very limited and consequently the total Nitrogen partial pressure used for depositing this hard coating has to be adjusted carefully.

The properties of CrN hard coatings are an excellent coefficient of friction, a relatively high hardness, its good oxidation resistance, and their chemical inertness. Thus these coating are predestinated for applications where a low friction coefficient is indispensable, such as forming tools, or applications with similar profiles of requirements [2, 5, 21].

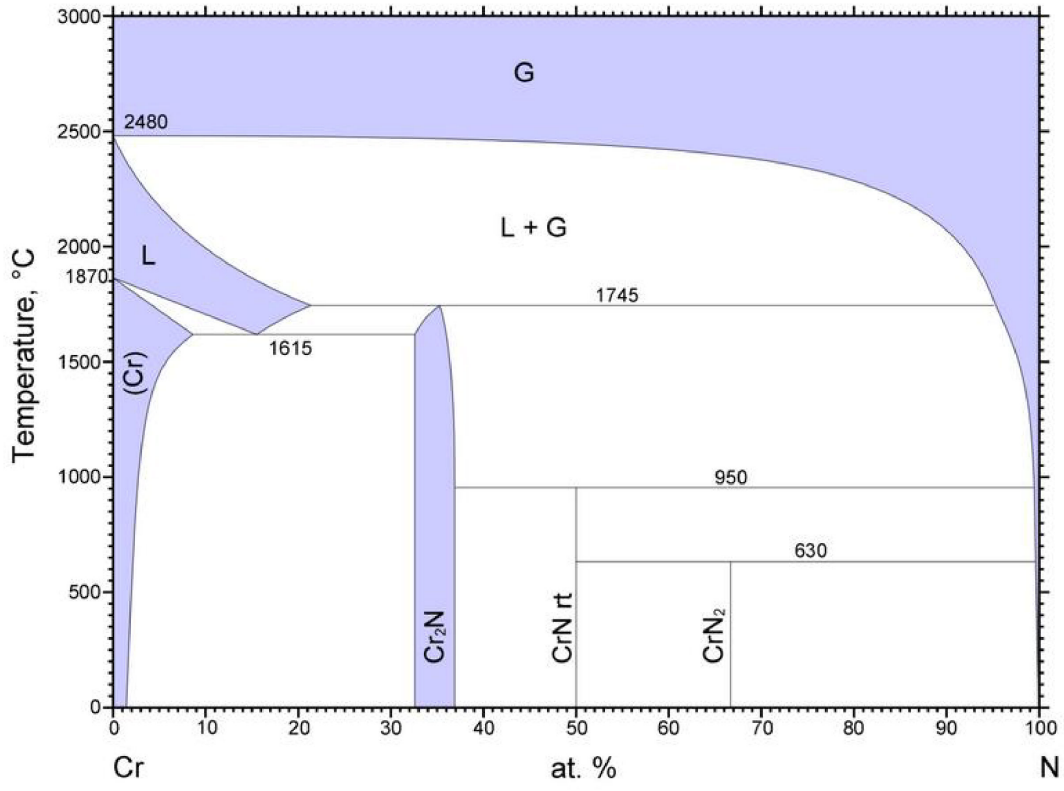

Figure 2.6: Binary phase diagram Cr-N [22].

2.5 Superlattice structures

Multilayered structures possess, compared to their monolithic counterparts, often advanced properties such as higher hardness, better chemical and thermal stability [23–26]. For example it was reported by Barshilia *et al.* [23] that a multilayered TiN/CrN system increased the thermal stability of the coating by about 150 °C compared to the monolithic coatings. This and other facts attracted the attention of researchers to investigate and improve such material systems.

In this work, the focus is on so called superlattice systems, layered coating systems with nanometer-range-thick single layers. The main effect of a superlattice structure on the mechanical properties was first predicted by Koehler *et al.* [27]. He postulated that, if a hypothetical layered material system possesses sufficient small layers and different shear moduli, Frank-Read sources will not be able to operate. Hence, the mechanical properties of this solid matter will enhance significantly. The theoretical work was experimentally confirmed for hard coatings by Helmersson *et al.* [26] for TiN/VN superlattice coatings. They deposited, using unbalanced magnetron sputtering, 1 μm thick hard coatings with differing bilayer periods. A maximum hardness peak of 5000 kg/m^2 was observed for $\Lambda = 4$ nm. A detailed explanation for the hardness (and mechanical properties) enhancement is given by Chu and Barnett [28]: They proposed two main mechanisms to be operative in superlattice coatings:

- Dislocation glide across interfaces: The dimensionless critical shear stress enhancement increases with increasing bilayer period, resulting in an impeded dislocation movement and thus an enhancement of the mechanical properties. This effect reaches a saturation value depending on the interface width. However, this effect is limited by the second mechanism:
- Dislocation glide within individual layers: When the stress required for dislocations to glide across layers is high enough, dislocation motion within the individual layer may occur. Primary this plastic deformation takes place in the layer with the lower shear modulus G. The stress required to move dislocation within the individual layers increases with decreasing bilayer periods.

Summarized, they concluded that the superlattice hardness depends on two parameters, namely the interface width and the difference of the shear moduli of the constituents.

2.6 Properties of TiN/CrN superlattice structures

As written in the latter chapters, TiN and CrN have almost the same lattice constant, a, differing only by 2%, and solidify in the same crystal structure (cubic B1). Therefore the TiN/CrN superlattice system is an iso-structural system (with a possible epitaxial growth), promoting a superlattice effect (increased mechanical properties due to predictions made by Koehler) because of their differing shear moduli. Barshilia *et al.* [29–31] intensively investigated the TiN/CrN superlattice system in recent years. They found for these structures, deposited with unbalanced magnetron sputtering, a peak hardness of roughly 37 GPa at a bilayer period of $\Lambda = 6\,\text{nm}$. The hardness of this system depends on several parameters, which can be varied by varying the deposition parameters. The bias-voltage for example is a major influencing parameter because of its impact on the morphology of the thin film.

The thermal stability of TiN/CrN superlattice system is limited to 800 °C which is also slightly higher than the thermal stability of the single layered materials. This can be explained by the formation of a dense Cr_2O_3 layer protecting the underlying thin film system and complex diffusion properties of O, N, Ti and Cr due to the multilayered structure [23].

Chapter 3

Methodical Approach

3.1 Coating preparation

The coatings were deposited using an AJA Orion 5 lab-scaled unbalanced magnetron sputtering system, illustrated with its main components in Fig. 3.1. This deposition plant uses a LabView based computer control system, which enables an automatized deposition process including pre-heating and pre-cleaning of the substrates and controlled shutter movement to obtain multilayered coating with a bilayer period in the nanometer range. Furthermore it is equipped with two 2 inch cathodes and one 3 inch cathode which can be powered by three dc-generators and one rf-generator. Additional dc- and rf-generators can be used for applying a bias voltage to obtain a denser coating morphology. The 6 inch rotating substrate holder can be heated up to 850 °C and varied in its vertical distance to the circular arrayed cathodes.

The TiN/CrN superlattice coatings were prepared at a deposition temperature of 500 °C and a vertical distance between cathodes and substrates of ~ 40 mm. Before depositing, the substrates (Si (100) $20 \times 7 \times 0.38\,\mathrm{mm}^3$) were ultrasonically cleaned in acetone and ethanol, for 5 minutes each, subsequently mounted in the deposition chamber and thermally cleaned for 20 minutes at 500 °C. After the cleaning procedure Ar-plasma etching was used for 10 minutes to remove a possible native Silicon-Oxide film. Therefore a voltage of -750 V and a chamber pressure of 6 Pa were used to create a sufficient high Ar-ion bombardment. The targets used in the process were high purity powder metallurgically produced targets (all from Plansee Composite Materials GmbH, 99.6 at.% purity) with a diameter of 3 inch and 2 inch for titanium and chromium, respectively. In order to obtain fully cubic CrN with no X-Ray diffraction (XRD)-indication of the hexagonal Cr_2N phase, a 1 : 1 gas mixture of Ar and N_2 with a total gas flow of 10 sccm (5 sccm each) was used within the whole process. Although an ideal Ar to N_2 ratio of 4 : 1 was found for TiN in the used deposition plant, the chosen gas mixture allowed growing TiN and CrN without changing the Ar to N_2 gas mixture.

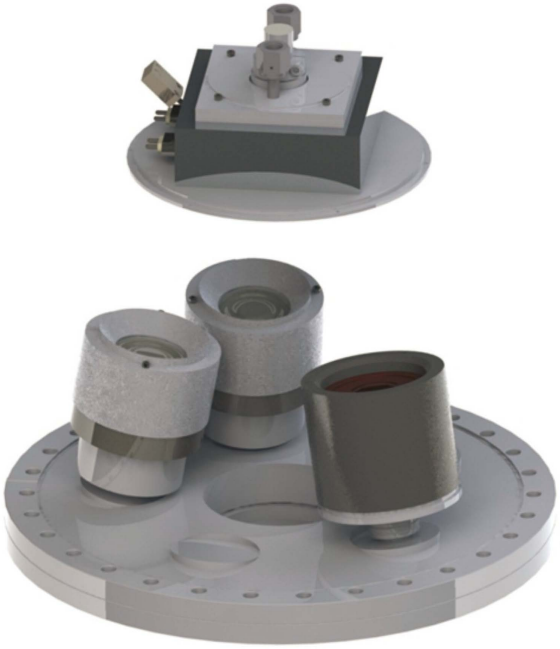

Figure 3.1: Schematic picture of the cathodes and the substrate holder (including the heating system) of an AJA Orion 5 deposition plant [14].

The base pressure of the coating chamber was at $\sim 5 \cdot 10^{-4}$ Pa, the gas pressure during the coating process was 0.4 Pa. The target power density was 6.8 W/cm^2 and 7.6 W/cm^2 for Titanium and Chromium respectively. To ensure a dense film morphology, a negative bias voltage of -60 V was applied to the substrates during the whole coating process [32]. As mentioned before, a computer controlled shutter system was used to control the thickness of the individual layers and to ensure a sharp interface between the TiN and CrN layers. All coatings (multilayer, superlattice, and monolithic) had a total thickness of $\sim 2.0\,\mu$m. The following bilayer periods were deposited: 186, 18.0, 13.2, 9.4, 8.6, 6.2, 4.0 and 1.8 nm.

3.2 Structural and chemical investigations

3.2.1 X-ray diffraction (XRD) and X-ray reflectivity (XRR)

X-Ray diffraction (XRD) is a method to obtain structural information of bulk materials, powders and thin films. Thereby a primary X-Ray beam is diffracted at certain lattice planes according to Bragg's law (see Eq. 3.1):

$$n \cdot \lambda = 2 \cdot d \cdot \sin(\Theta) \tag{3.1}$$

where λ donates the wavelength of the primary X-Ray radiation, n the order of the peak, d the lattice parameter and Θ the angle between the sample surface and the detector. The emerging radiation is then quantified by a detector.

In this thesis High angle X-Ray diffraction analysis (HAXRD) experiments in Bragg-Brentano configuration of as-deposited thin films were conducted between 2Θ angles of 30 ° and 90 ° in order to identify the phases. Therefore a PANalytical Empyrean diffractometer equipped with a Cu-K_α radiation source ($\lambda = 1.54056\,\text{nm}$) and a PIXcel1D point detector were used.

Furthermore, to calculate the bilayer period and compare these calculated values with the nominal ones, X-Ray reflectivity (XRR) measurements were performed. Therefore the diffractometer was calibrated to ensure a precise parallel alignment between the X-Rays and the thin film surface. Each bilayer period was measured 10 times and afterwards added up to obtain a good peak quality. The bilayer period was calculated by following modified Bragg's law approach:

$$\Lambda = \frac{m \cdot \lambda}{2 \cdot \sin(\Theta)} \tag{3.2}$$

In this case m donates the order of the satellite peak, Λ the bilayer period, and λ and Θ, the wavelength of the used radiation and the angle between the sample surface and the detector respectively. For further information of the evaluation of the bilayer period by X-ray reflectivity and general information on X-ray diffraction the reader is referred to Ref. [33].

3.2.2 Scanning electron microscopy (SEM)

Cross sectional images of the monolithic and superlattice thin films were taken by a FEI Quanta 200 FEG (operating at an acceleration voltage of 10 kV) to investigate and evaluate the film morphology, microstructure and the overall film thickness. In order to obtain a brittle fracture surface without any plastic deformation the substrates were broken in a way to avoid compressive stress. In addition the SEM was used to determine the actual beam dimensions before the fracture tests and to estimate the initial crack depth. After the in-situ micromechanical cantilever bending tests, SEM was used to measure the exact initial crack length and for a qualitative evaluation of the fracture surface. The *in-situ* tests itself were conducted in a JEOL JSM 6430 SEM, operating at an acceleration voltage of 5 kV. The basic principle of SEM-imaging can be explained by an interaction between accelerated electrons and the surface of the sample (in this case the emission of secondary electrons) and subsequent computer-assisted detection and processing [34].

3.2.3 Focused ion beam (FIB)

For the preparation of the micro-cantilevers a FEI Quanta dual beam FIB was used. The basic principle of ion-imaging resembles that of electron imaging, but instead of electrons, in this case Ga-ions are used for imaging and material-erosion. This instrument combines both, an ion beam column for the milling process and an electron beam column in order to monitor the latter. The ion column was operated at an acceleration voltage of 30 kV. During the

milling process of the cantilevers the acceleration current of the Gallium-ions was reduced to 500 pA to avoid beam damage and subsequent influence on the material properties [35]. The pre-notch was created using an acceleration current of 50 pA to obtain a well-defined sharp crack shape.

3.2.4 Transmission electron microscopy (TEM)

The use of TEM enables detailed structural investigations of material systems, down to a resolution of several Ångström. By reason of these detailed insights into the matter a qualitative evaluation of the interface quality (width) is provided. The sample preparation was carried out by polishing the coated silicon substrate down to a thickness of $\sim 10\,\mu$m and a following Ar-ion polishing treatment using a GATAN PIPS (precise ion polishing system) to thin out the sample down to the necessary thickness of some ten nanometers. The investigations of the samples used in this thesis were carried out in a FEI TECNAI F20 HRTEM (high resolution transmission electron microscope) operating at an acceleration voltage of 200 kV [34].

3.3 Mechanical investigations

3.3.1 Nanoindentation

Hard coatings require, due to their small dimensions (in this case the thickness of the films was, as mentioned before, $\sim 2.0\,\mu$m), certain measure conditions for the determination of their hardness. All these requirements are met with using nanoindentation. The hardness measurements in this thesis were performed with an UMIS Nanoindenter from Fisher-Cripps Laboratories equipped with a Berkovich indenter. During the loading and unloading process a load-displacement curve was recorded, enabling an indentation-hardness determination according to Oliver and Pharr [36]. For every sample 30 load controlled single-indentations with loads between 25 mN and 2 mN were performed. For the calculation of the hardness only measurements with a total indentation depth lower than 10% of the film thickness were taken into consideration, to avoid a possible substrate influence. Measurements with low indentation depths were not evaluated due to the affections by the surface roughness. The indentation modulus E^* can be calculated by analyzing the unloading curve. A schematic load-displacement curve including the most important values for calculating both, the indentation hardness and the indentation modulus, is given in Fig. 3.2. The hardness values showed a typical curve shape for superlattice thin films (H vs. Λ, see Fig. 3.6). A detailed description on the indentation and the evaluation of hardness and indentation modulus including a critical review on the derived values can be found in literature [37, 38].

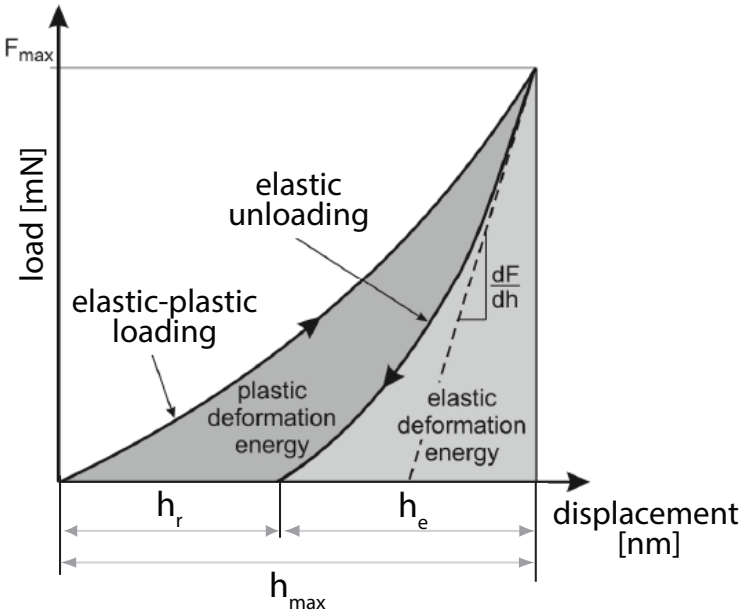

Figure 3.2: Load/displacement curve [39].

3.3.2 Fracture toughness

In recent years various testing methods have been developed for calculating or estimating the fracture toughness of thin films, including tensile tests [40], four-point bending tests [41] and indentation test [42]. Due to the proportianal small examined sample volume (coating to substrate), one has to take into account that some of these experiments are only able to estimate the fracture toughness or compare different ceramic hard coating systems. Exceptions from these rules are for example the double cantilever bending test, the pillar splitting test, the clamped beam bending test and the single cantilever bending test. In this thesis single cantilever bending tests were performed by reason of their high success rate, the relatively simple preparation and execution and the assurance of mode I conditions [9]. The differences between mode I, mode II and mode III conditions are given in Fig. 3.3. The sample preparation, the experimental procedure and the evaluation/calculation of the fracture toughness K_{IC} from the obtained raw data will be described in more detail in following chapters.

Sample preparation

Prior to the FIB-milling of the cantilevers a freestanding thin film with a width of $\sim 20\,\mu$m had to be produced. This freestanding ceramic coating guarantees the absence of substrate and residual stress, a necessary precondition for determining correct fracture toughness values. Before the removal of the substrates from the thin film, they were broken in a way that exclusively tensile stresses occur in the coating during the breaking to eliminate any possible plastic deformation. Afterwards the substrates were etched in aqueous potassium hydroxide

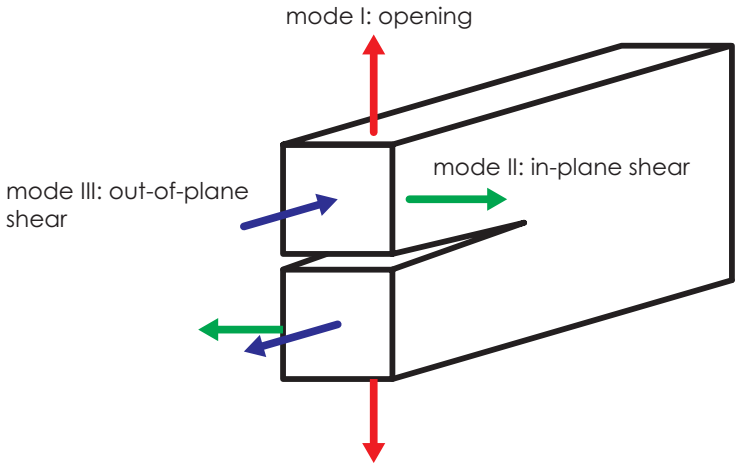

Figure 3.3: Illustration of the three different loading modes.

solution with a concentration of 30 wt.% (KOH) at a temperature of 60 °C for one and a half hour. It is worth mentioning that etching of silicon in KOH is anisotropic, i.e., that the etching rate depends on the crystallographic direction. For the selected parameters the etching rate in direction of the (100) plane is about 100 times higher than that of the (111) direction, resulting in a typical appearance of the freestanding film schematically shown in Fig. 3.4.

As already stated before and in Chapter 3.2.3, cantilevers were created out of the freestanding thin film by FIB-milling. Prior to this step the etched substrates were glued onto a sample holder, guaranteeing a perpendicular alignment of the thin film surface to the loading axis, and electrically connected with conductive silver. The dimensions of the cantilevers used for micromechanical testing were approximately following: the length l was 7 times the thin film thickness w, the width b was equal to w and the length of the initial crack was chosen 0.75 times w. The depth a of the initial crack should had been, in all of the different thin films by cause of their similar thickness, about 300 nm. As one cannot measure this dimension before the micromechanical tests, pretests were conducted to figure out the required milling

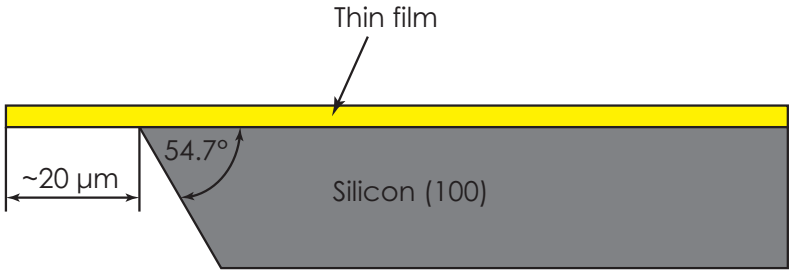

Figure 3.4: Illustration of etched substrate.

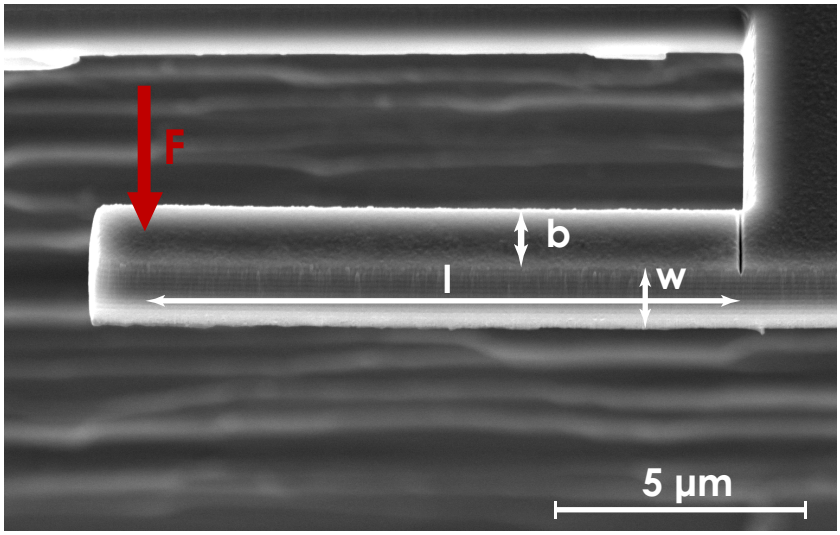

Figure 3.5: SEM picture of a cantilever before micromechanical testing.

time. Before loading the cantilevers in the micromechanical tests, their final dimensions were measured using a SEM. A 45 ° inclined SEM picture of one of those cantilevers is shown in Fig. 3.5.

In-situ micromechanical testing

The *in-situ* bending tests of the freestanding cantilevers were performed in a JEOL JSM 6430 scanning electron microscope equipped with an UNAT SEM-2 nanoindenter. The nanoindenter was equipped with a 2.0 μm spherical diamond tip to avoid unintended shear and torsion loadings as well as plastic deformation of the samples. The micromechanical experiments were carried out in a displacement controlled mode with a displacement rate of $\sim$ 5 nm/s until catastrophic failure. Per thin film system 10 micro-cantilevers were tested, the average success rate was $\sim$ 76%. During these experiments the load and the displacement of the indenter were recorded, showing an ideal linear elastic deformation behavior of the beams, thus allowing the calculation of mode I fracture toughness values (K_{IC}).

Calculation of the fracture toughness K_{IC}

The following formula (Eq. 3.4) was used to calculate the fracture toughness of the thin films:

$$K_{IC} = \frac{P_{max} \cdot l}{b \cdot w^{3/2}} \cdot f\left(\frac{a}{w}\right) \tag{3.3}$$

with a geometry factor $f\left(\frac{a}{w}\right)$ of:

$$f\left(\frac{a}{w}\right) = 1.46 + 24.36 \cdot \left(\frac{a}{w}\right) - 47.21 \cdot \left(\frac{a}{w}\right)^2 + 75.18 \cdot \left(\frac{a}{w}\right)^3 \tag{3.4}$$

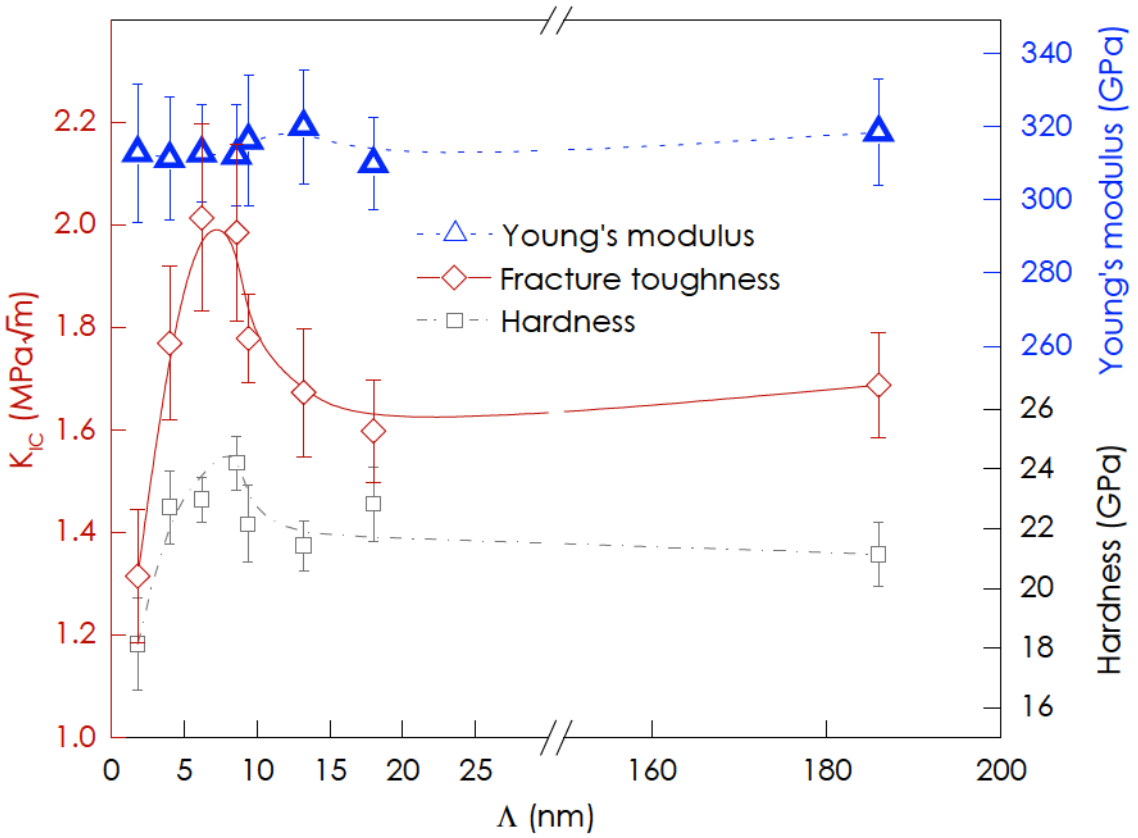

Figure 3.6: Data derived from nanoindentation and micromechanical experiments.

according to Matoy *et al.* [43]. P_{max} donates the maximum force measured during the micromechanical testing. Interestingly, the obtained K_{IC} values show an almost identical curve progression as the hardness values, which will be discussed more detailed in Publication I.

Bibliography

[1] B. Denkena and H. K. Toenshoff, *Spanen: Grundlagen* (Springer-Verlag, 2011).

[2] A. Anders, *Cathodic Arcs: From Fractal Spots to Energetic Condensation* (Springer Science & Business Media, 2009).

[3] W. D. Sproul, J. Vac. Sci. Technol. A **12**, 1595 (1994).

[4] S. Zhang, D. Sun, Y. Fu, and H. Du, Surf. Coat. Technol. **198**, 2 (2005).

[5] Powder Diffraction File 00-011-0065, International Centre for Diffraction Data (1958).

[6] Powder Diffraction File 00-038-1420, International Centre for Diffraction Data (1987).

[7] Z. Xia, W. A. Curtin, and B. W. Sheldon, Acta Mater. **52**, 3507 (2004).

[8] S. Liu, J. M. Wheeler, P. R. Howie, X. T. Zeng, J. Michler, and W. J. Clegg, Appl. Phys. Lett. **102**, 171907 (2013).

[9] B. N. Jaya, C. Kirchlechner, and G. Dehm, J. Mater. Res. **30**, 686 (2015).

[10] P. M. Martin, *Handbook of Deposition Technologies for Films and Coatings: Science, Applications and Technology* (Elsevier Science, 2009).

[11] P. H. Mayrhofer, *Materials science aspects of nanocrystalline PVD hard coatings*, Ph.D. thesis, Montanuniversität Leoben (2001).

[12] G. Dhanaraj, K. Byrappa, V. Prasad, and M. Dudley, *Springer Handbook of Crystal Growth*, Springer Handbook of Crystal Growth (Springer Berlin Heidelberg, 2010).

[13] A. Anders, Thin Solid Films **518**, 4087 (2010).

[14] M. Schlögl, *Multilayer design for increased toughness of CrN-based coatings*, Ph.D. thesis, Montanuniversität Leoben (2012).

[15] W. Münz, J. Vac. Sci. Technol. A **4**, 2717 (1986).

[16] J. Vetter, E. Lugscheider, and S. S. Guerreiro, Surf. Coat. Technol. **98**, 1233 (1998).

[17] H. Riedl, D. Holec, R. Rachbauer, P. Polcik, R. Hollerweger, J. Paulitsch, and P. H. Mayrhofer, Surf. Coat. Technol. **235**, 174 (2013).

[18] A. Mumtaz and W. H. Class, Journal of Vacuum Science & Technology **20**, 345 (1982).

[19] A. Münster, Angew. Chem. Int. Ed Engl. **69**, 281 (1957).

[20] H. Ohtani and M. Hillert, CALPHAD **14**, 289 (1990).

[21] J. Vetter, R. Knaup, H. Dweletzki, E. Schneider, and S. Vogler, Surf. Coat. Technol. **86-87**, 739 (1996).

[22] http://materials.springer.com/isp/phase-diagram/docs/c_0902610, accessed: 2016-6-4.

[23] H. C. Barshilia, A. Jain, and K. S. Rajam, Vacuum **72**, 241 (2003).

[24] L. Hultman, C. Engström, and M. Odén, Surf. Coat. Technol. **133–134**, 227 (2000).

[25] J.-K. Park and Y.-J. Baik, Surf. Coat. Technol. **200**, 1519 (2005).

[26] U. Helmersson, S. Todorova, S. A. Barnett, J. E. Sundgren, L. C. Markert, and J. E. Greene, J. Appl. Phys. **62**, 481 (1987).

[27] J. S. Koehler, Phys. Rev. B Condens. Matter **2**, 547 (1970).

[28] X. Chu and S. A. Barnett, J. Appl. Phys. **77**, 4403 (1995).

[29] H. C. Barshilia and K. S. Rajam, Bull. Mater. Sci. **26**, 233 (2003).

[30] H. C. Barshilia and K. S. Rajam, J. Mater. Res. **19**, 3196 (2004).

[31] H. C. Barshilia, N. Selvakumar, K. S. Rajam, K. Gopinadhan, and S. Chaudhary, J. Phys. D Appl. Phys. **41**, 205409 (2008).

[32] D. S. Rickerby and P. J. Burnett, Thin Solid Films **157**, 195 (1988).

[33] L. Spieß, G. Teichert, R. Schwarzer, H. Behnken, and C. Genzel, Vieweg+ Teubner (2009).

[34] M. v. Heimendahl, *Einführung in die Elektronenmikroskopie-Verfahren zur Untersuchung von Werkstoffen und anderen Festkörpern* (Friedr. Vieweg & Sohn, Braunschweig, 1970).

[35] L. A. Giannuzzi and N. C. S. University, *Introduction to Focused Ion Beams: Instrumentation, Theory, Techniques and Practice* (Springer Science & Business Media, 2006).

[36] W. C. Oliver and G. M. Pharr, J. Mater. Res. **7**, 1564 (1992).

[37] A. C. Fischer-Cripps, Surf. Coat. Technol. **200**, 4153 (2006).

[38] A. C. Fisher-Cripps, "Nanoindentation (mechanical engineering series)," (2004).

[39] W. D. Nix, Materials Science and Engineering: A **234**, 37 (1997).

[40] L. Qian, S. Zhu, Y. Kagawa, and T. Kubo, Surf. Coat. Technol. **173**, 178 (2003).

[41] A. K. Ray and R. W. Steinbrech, J. Eur. Ceram. Soc. **19**, 2097 (1999).

[42] S. Bhowmick, R. Bhide, M. Hoffman, V. J. *, and S. K. Biswas, Philos. Mag. **85**, 2927 (2005).

[43] K. Matoy, H. Schönherr, T. Detzel, T. Schöberl, R. Pippan, C. Motz, and G. Dehm, Thin Solid Films **518**, 247 (2009).

Chapter 4

Publications

Publication I

Superlattice effect for enhanced fracture toughness of hard coatings
R. Hahn, M. Bartosik, R. Soler, C. Kirchlechner, G. Dehm, P.H. Mayrhofer
Manuscript submitted to Scripta Materialia.

Superlattice effect for enhanced fracture toughness of hard coatings

R. Hahn,[1,*] M. Bartosik,[1] R. Soler,[2] C. Kirchlechner,[2] G. Dehm,[2] and P.H. Mayrhofer[1]

[1] *Institute of Materials Science and Technology, TU Wien, A-1060 Vienna, Austria*
[2] *Max-Planck-Institut fr Eisenforschung, Max-Planck-Straße 1, D-40237 Düsseldorf, Germany*

(Dated: June 12, 2016)

Coherently grown nanolayered TiN/CrN thin films exhibit a superlattice effect in fracture toughness, similar to the reported effect in indentation hardness. We found – by employing *in-situ* micromechanical cantilever bending tests on free-standing TiN/CrN superlattice films – that the fracture toughness increases with decreasing bilayer period (Λ), reaching a maximum at $\Lambda \sim 6\,$nm nm. For ultrathin layers ($\Lambda \sim 2\,$nm), the fracture toughness drops to the lowest value due to intermixing and loss of superlattice structure. Both, fracture toughness and hardness peak for similar bilayer periods of TiN/CrN superlattices.

Keywords: fracture toughness; superlattice toughness; nanolayer; hard coatings; micromechanical testing.

Hard coatings are used to protect engineering components, e.g. cutting tools, from severe external loads and harsh environments [1]. Thereby, the coatings should be ideally strong and tough. Multilayer coatings composed of two coherently stacked, alternating materials with a periodicity length in the nanometer range, referred to as superlattice films, have been reported to possess exceptional high hardness values exceeding that of their single layered constituents by some hundred percent. In the 1980s, Helmersson *et al.* [2] reported on a hardness enhancement of up to $\sim 250\%$ compared to single-layered materials for the single-crystalline coherent TiN/VN superlattice (SL) structure grown by physical vapor deposition on single crystalline MgO (100) substrates. Thereby, the peak hardness was found for a periodicity length of $\sim 5\,$nm. Later, an hardness enhancement was observed for a row of other SL film systems grown on MgO (100), but also on (native oxide) of Si (100) and polycrystalline steel substrates [3].

Besides high hardness values, a sufficiently high fracture toughness is needed to ensure the integrity of bulk and coated engineering components. Unfortunately, these material properties are commonly mutually influential (especially for materials showing plastic behavior), as a high strength often implies a low fracture toughness and *vice versa* [4]. In the last decades various strategies have successfully shown how to break down this relationship, spanning from grain refinement toughening – based on the classical Hall-Petch relation used in a variety of steels [5, 6] – to recently found nanoscaled twinning mechanisms being operative in high-entropy alloys – enabling exceptional high fracture-resistance even at cryogenic temperatures [7] – and several other mechanisms presented in Ref. [4]. Strategies for enhancing the (fracture) toughness of ceramic coatings (see review by Zhang *et al.* [8]) include: incorporating a ductile phase; toughening through a nanocrystalline microstructure, composition, or structure grading; multilayer structuring; phase transformation toughening; or apparent toughening by implementation of compressive stresses, most of them being already effectively applied in industrial products. However, the exceptional effect of a superlattice structure on the fracture toughness has yet not been reported. Here, we study the influence of the superlattice structure on the fracture toughness. Therefore, we have conducted micromechanical experiments on freestanding superlattice coatings with different bilayer periods (Λ). The isomorphous face-centered cubic (B1) TiN/CrN superlattice grown on Si (100) substrates served as a model system. The constituents TiN and CrN represent one of the most widely used nitrogen-based hard coating materials and their shear moduli ($\sim 180\,$GPa [9] and $\sim 135\,$GPa [10], respectively) are significantly different, which promotes the superlattice effect [11].

TiN/CrN multilayer films with equal thick layers – bilayer periods ranging from 2 to 200 nm, and total film thicknesses of $2\,\mu$m were synthesized by dc unbalanced reactive magnetron sputtering. All films were grown on Si (100) substrates ($7 \times 20 \times 0.38\,\text{mm}^3$) in an AJA International Orion 5 magnetron sputtering system equipped with one two-inch Cr and one three-inch Ti target (both from Plansee Composite Materials GmbH, 99.6*at.*% purity). Prior to the deposition, the substrates were ultrasonically cleaned in ethanol and acetone, for 5 minutes each. Subsequently, the substrates were mounted inside the deposition chamber (evacuated to a base pressure below $10^{-4}\,$Pa), thermally cleaned at $500\,^{\circ}$C for 20 min, and Ar-plasma etched (Ar pressure = 6 Pa) at the same temperature for 10 min. The deposition was carried out at $500\,^{\circ}$C in an Ar/N_2 gas mixture with a flow ratio of 1/1 and a total pressure of 0.4 Pa. Both targets were dc powered using a target power density of $6.8\,\text{W/cm}^2$ for Ti and $7.6\,\text{W/cm}^2$ for Cr. To ensure a dense film morphology, a constant negative bias potential of $-60\,$V was applied to the substrates. The alternating and equally thick TiN and CrN layers were deposited by using a computer controlled shutter system mounted in front of the Ti and Cr targets. Films with the following nominal bilayer periods (obtained by dividing the total film thickness with the number of TiN/CrN pairs) were synthesized: 1.8, 4.0, 6.2, 8.6, 9.4, 13.2, 18.0, and 186 nm. To

* rainer.hahn@tuwien.ac.at

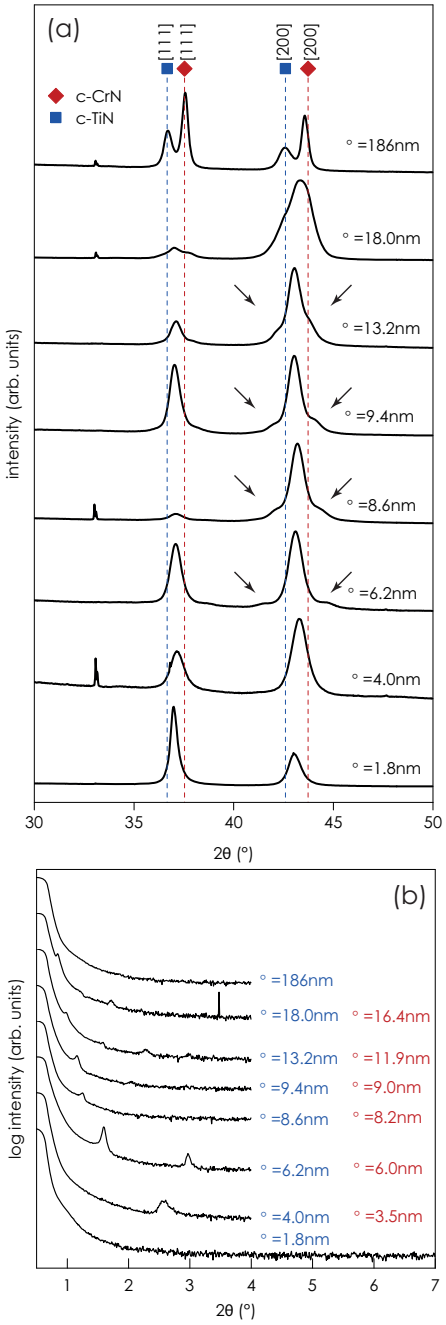

FIG. 1. XRD (a) and XRR (b) scans of TiN/CrN superlattice films with different bilayer periods Λ. The arrows in (a) exemplarily mark satellite peaks in the vicinity of the 200 Bragg peak reflecting the SL structure. The bilayer periods quoted in the left column (blue) in (b) were calculated by dividing the total film thickness through the number of TiN/CrN pairs (obtained from the computer controlled deposition system), those in the right column (red) were calculated from the 2Θ peak-positions. The coatings with the thickness-obtained Λ of 1.8 nm and 186 nm show no signs of a superlattice structure.

highlight the superlattice effect itself, we intentionally used only a moderate bias potential of −60 V during the deposition of our polycrystalline TiN/CrN thin films, although Barshilia *et al.* [12], for instance, reported even higher peak hardnesses for TiN/CrN superlattice films when prepared with high bias potentials of −150 V.

X-ray diffraction (XRD) patterns from all coatings were collected in symmetric Bragg-Brentano configuration using Cu-K_α radiation and are presented in Fig. 1(a). The XRD patterns show that the films grew in the face-centered cubic crystal structure. Cumulative diffraction peaks with peak positions laying in between TiN and CrN peaks (instead of two clearly differentiate peaks) reveal the presence of a superlattice structure with strained layers. Furthermore, positive and negative satellite peaks reflecting the SL structure (marked exemplarily with arrows in Fig. 1(a) in the vicinity of the 200 Bragg peak) emerge for the $\Lambda = 6.2$ nm multilayer film and become more apparent with increasing bilayer period. In the case of the multilayer film with the thickest bilayer period ($\Lambda = 186$ nm), two clearly separated Bragg peaks matching TiN and CrN lattice constants are observed, suggesting a largely independent growth of TiN and CrN layers with incoherent or semi-coherent interfaces, as expected for large bilayer periods. The native oxides on the Si (100) substrates lead to the formation of a polycrystalline structure within all our thin films.

In order to confirm the estimated nominal bilayer periods we conducted X-ray reflectivity (XRR) measurements, Fig. 1(b), and used a modified Braggs-law approach to calculate Λ:

$$\sin^2(\Theta) = \left(\frac{m \cdot \lambda}{2 \cdot \lambda}\right)^2 + 2 \cdot \delta, \qquad (1)$$

where m denotes the order of the reflection, λ the wavelength of radiation (here Cu-K_α) and δ the real part of the average refractive index (in our case $\delta \sim 1.6 \cdot 10^{-5}$ [13]. The XRR obtained bilayer periods excellently fit to the nominal bilayer periods, see the listed values in Fig. 1(b). The XRR patterns show no signs for a superlattice structure for our thin films with the largest and smallest nominal bilayer periods ($\Lambda = 186$ and 1.8 nm), hence, no XRR obtained bilayer periods could be calculated for these. This suggests that for our thin film with the smallest nominal bilayer period of 1.8 nm, the intermixing interface regions between TiN and CrN layers are too dominant to allow for the development of a superlattice structure. These results are further supported by transmission electron microscopy (TEM) cross section images, Figs. 2(a) and (b). In contrast to our thin film with a nominal Λ of 13.2 nm (exhibiting a pronounced superlattice structure) no layered structure can be observed for the sample with a nominal Λ of 1.8 nm, explaining the missing XRR peak. The TEM samples were prepared by conventional grinding of a film-substrate lamella down to a thickness of $\sim 10\,\mu$m using a diamond abrasive. A GATAN Precise Ion Polishing System was used to further thin the sample down till electron transparency. The

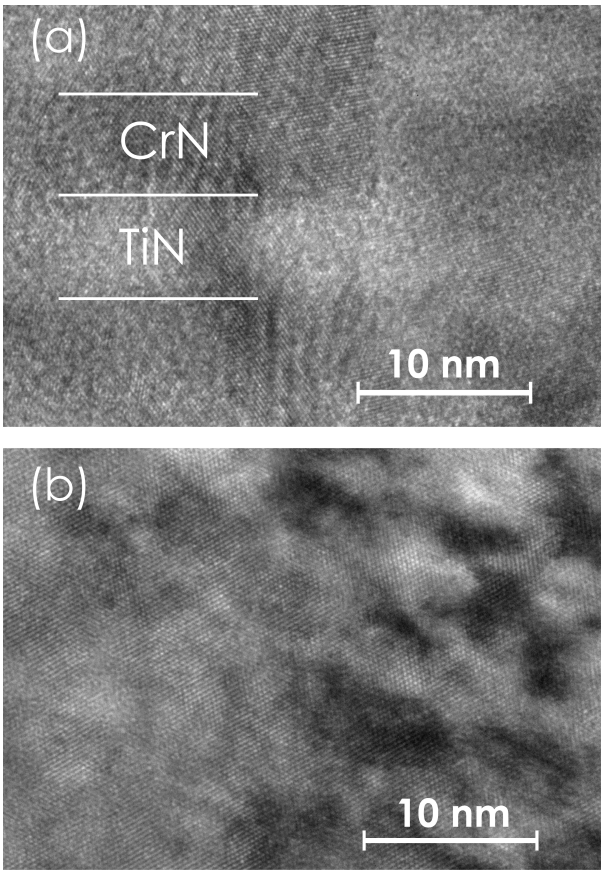

FIG. 2. HR-TEM images of the TiN/CrN superlattice films exhibiting bilayer periods of 13.2 (a) and 1.8 nm (b), respectively. While the nanolayered structure can be clearly seen for the large bilayer period sample (a) the interdiffusion-areas between TiN and CrN and loss of the layer structure becomes evident for the smallest bilayer period samples shown in (b).

TEM-images were recorded using a FEI TECNAI F20 operating with an acceleration voltage of 200 kV. To determine the fracture toughness of all TiN/CrN thin films, micromechanical single cantilever bending tests were performed on free-standing films. This approach allows to effectively eliminate potential sources of errors, like the influence of the substrate material and residual film stresses on the fracture toughness [14]. The Si substrates were locally dissolved by 90 min wet chemical etching in a 30 wt.% potassium hydroxide (KOH) solution heated to 60 °C. As a result, freestanding films ($\sim 20\,\mu$m broad and a few mm wide) were obtained. Cantilevers with dimensions of $\sim 2 \times 2 \times 14\,\mathrm{m}^3$ were fabricated by Ga^+ focused ion beam (FIB) milling perpendicular to the film surface, using a FEI Quanta 200 3D DBFIB work station. A final milling current of 500 pA at an acceleration voltage of 30 kV was employed. The pre-notch was milled using 50 pA. A scanning electron microscope image (30 ° inclined from top view) of a pre-notched single cantilever specimen after FIB milling is depicted in Fig. 3(a).

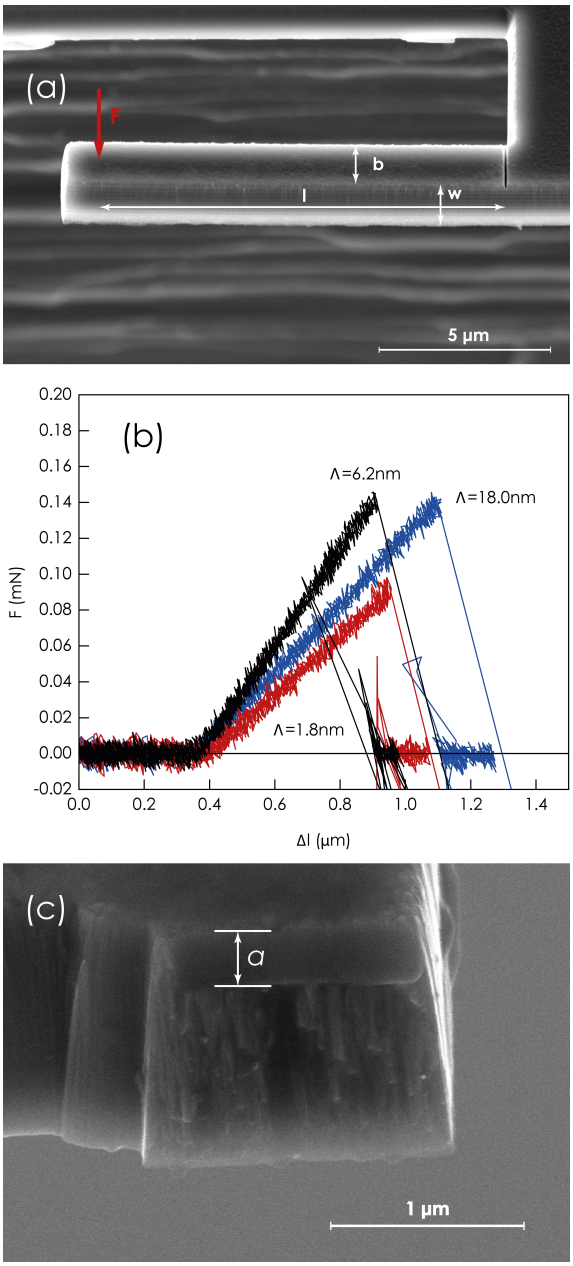

FIG. 3. (a) Scanning electron microscope image (30 ° inclined from top view) of a pre-notched single cantilever specimen before micromechanical testing, (b) representative bending stress-deflection curves recorded in the micromechanics single cantilever bending experiments from TiN/CrN superlattice films with bilayer periods of 1.8, 6.2 and 18.0 nm, (c) SEM micrograph of fracture surface showing pre-notch depth a.

The in-situ micromechanical experiments were performed in a JEOL scanning electron microscope (JEOL JSM 6430, JEOL Ltd., Akishima, Japan) equipped with an UNAT SEM-2 nanoindenter (ASMEC GmbH, Radeberg, Germany). A 2 μm spherical diamond tip was used

for the experiments. The tests were carried out on a displacement-controlled mode, at a constant displacement rate of 5 nm/s. For each multilayer film system, 10 micro-beams were tested (with an average success rate of $\sim 76\%$). Representative load-deflection curves for the SL films with $\Lambda = 1.8, 6.2$, and 18.0 nm are shown in Fig. 3(b). Note that deviations on loading stiffness arise for different cantilevers due to small variations on actual cross-sections and distances of applied load, l. Nonetheless, all SL structures present a perfect linear-elastic brittle fracture behavior without any signs of plasticity in the load-displacement response. Therefore, linear-elastic fracture mechanics was applied to quantify the fracture toughness K_{IC}:

$$K_{IC} = \frac{P_{max} \cdot l}{b \cdot w^{3/2}} \cdot f\left(\frac{a}{w}\right), \tag{2}$$

whereby the geometry factor $f\left(\frac{a}{w}\right)$ was taken as:

$$f\left(\frac{a}{w}\right) = 1.46 + 24.36 \cdot \left(\frac{a}{w}\right) - 47.21 \cdot \left(\frac{a}{w}\right)^2 + 75.18 \cdot \left(\frac{a}{w}\right)^3, \tag{3}$$

according to Matoy *et al.* [15]. P_{max} denotes the maximum force, l the lever arm, b the width of the cantilever, and w the film thickness (see Fig. 3(a)). The initial crack length, a, was determined from SEM micrographs of the post mortem fracture surface, as shown in an example in Fig. 3(c). The relatively flat fracture surface together with the absence of dimples or any other sign of significant plastic deformation, confirm the brittle fracture response of our thin films.

The derived fracture toughness (K_{IC}) vs. the bilayer period for all superlattices studied – as well as those of the thin films with a nominal Λ of $\sim$ 186 and 1.8 nm – is presented in Fig. 4 showing a pronounced bilayer-period-dependent behavior. For large bilayer periods ($\Lambda \geq 13$ nm), K_{IC} remains relatively constant, at $\sim 1.65 \pm 0.1\,\mathrm{MPa} \cdot \mathrm{m}^{1/2}$. For smaller bilayer periods, K_{IC} significantly raises, reaching a maximum value of $\sim 2.01 \pm 0.18\,\mathrm{MPa} \cdot \mathrm{m}^{1/2}$ at $\Lambda \sim 6.2$ nm. Further decreasing Λ drops dramatically K_{IC} to a minimum value of $\sim 1.31 \pm 0.13\,\mathrm{MPa} \cdot \mathrm{m}^{1/2}$ at $\Lambda \sim 1.8$ nm. Interestingly, a very similar dependency is observed for the hardness measurements, with H vs. Λ exhibiting a hardness peak with 24.2 ± 0.9 GPa at $\Lambda \sim 8.6$ nm. The agreement between K_{IC} vs. Λ and H vs. Λ suggests that similar bilayer-period-dependent mechanisms are responsible for both, the indentation hardness and the fracture toughness enhancement. The relatively constant indentation modulus as a function of the bilayer period, E vs. Λ, further proofs our K_{IC} vs. Λ curve by the coincidence with the H/E empirical criteria, often used to qualitatively rate materials for their toughness [16, 17]. The higher the hardness of brittle materials, the higher should be the energy absorbed until fracture, if their E values are similar.

The hardness enhancement due to the superlattice effects, described by the model after Chu and Barnett [18], is based on two mechanisms being operative during plastic deformation of a superlattice system. For small bilayer periods, the stresses required for dislocations to glide across layers with different shear moduli increase with increasing bilayer periods. The second mechanism describes the stress required to move preexisting dislocations within the layers, as well as the stress required to activate dislocation sources. The latter two required stresses, τ, decrease with increasing bilayer period, following a Hall-Petch-like relationship:

$$\tau \propto \Lambda^{-m}. \tag{4}$$

Hardness enhancement due to the superlattice effect is, therefore, a plasticity driven phenomenon, and as such, is governed by dislocation mobility. In contrast, fracture in linear-elastic brittle materials is characterized for having little to non-plastic deformation, and be controlled by the average defect density and average maximum defect size. Thereby, rather than a bilayer-period-dependent dislocation-based mechanism, there must be an underlying bilayer-period-dependent property governing both SL effects. Some of these bilayer-period-dependent properties might be: coherency strains; misfit dislocation arrays at the interface; spatially oscillating elastic moduli influencing crack growth; average grain size and other defects confined into individual layers. The decline in H as well as K_{IC} when further reducing the bilayer period (below ~ 6 nm) is also based on the decreasing SL effect, as with smaller bilayer periods the intermixing interface-regions between both layer types become dominant see Figs. 1(b) and 2(b) and the missing signs for a superlattice structure with a nominal Λ of 1.8 nm.

It is yet to be discovered which intrinsic SL property is responsible for the fracture toughness enhancement. But based on our results, a power-law relationship similar as

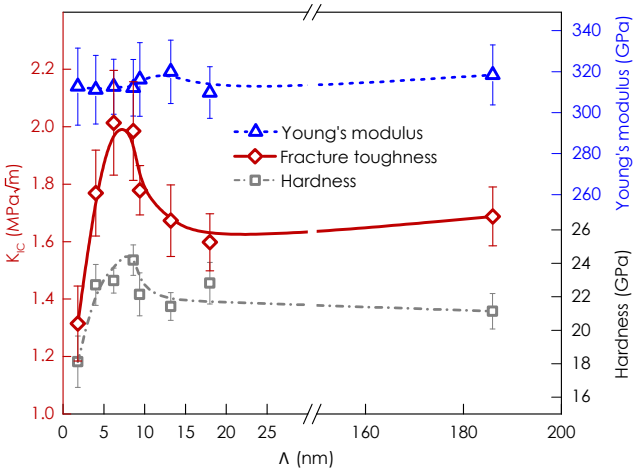

FIG. 4. Fracture toughness K_{IC}, indentation hardness H and moduli E of our TiN/CrN superlattice thin films as a function of their bilayer period Λ. The individual data points are connected to guide the eye.

for τ will hold between the fracture toughness and the bilayer period:

$$K_{IC} \propto \Lambda^{-m}, \tag{5}$$

with the exponent m depending on the type and interface constitution of the superlattice structure. The exponent m equals roughly 0.25 for our superlattice TiN/CrN coatings with $\Lambda \geq 6.2\,\mathrm{nm}$.

Based on our results on polycrystalline TiN/CrN SL structures – deposited by unbalanced magnetron sputtering with different bilayer periods on Si (100) substrates – we can conclude, that a significant increase in fracture toughness is observed when SL structures are formed, similar to the well-known SL effect on hardness. This new superlattice effect represents a significant improvement in mechanical properties of hard thin films, especially when both, hardness and fracture toughness, are simultaneously enhanced as it is the case here.

The financial support by the START Program (Y371) of the Austrian Science Fund (FWF) is gratefully acknowledged. SEM, TEM, and XRD investigations were carried out using facilities of the XRC and USTEM centers of TU Wien, Austria. The work of RS has been conducted within the project EPPL, co-founded by grants from Austria, Germany, The Netherlands, France, Italy, Portugal and the ENIAC Joint Undertaking.

[1] P. H. Mayrhofer, A. Hörling, L. Karlsson, J. Sjölén, T. Larsson, C. Mitterer, and L. Hultman, Appl. Phys. Lett. **83**, 2049 (2003).
[2] U. Helmersson, S. Todorova, S. A. Barnett, J. E. Sundgren, L. C. Markert, and J. E. Greene, J. Appl. Phys. **62**, 481 (1987).
[3] M. Stueber, H. Holleck, H. Leiste, K. Seemann, S. Ulrich, and C. Ziebert, J. Alloys Compd. **483**, 321 (2009).
[4] R. O. Ritchie, Nat. Mater. **10**, 817 (2011).
[5] J. W. Morris, Jr, Lawrence Berkeley National Laboratory (2001).
[6] M. Calcagnotto, D. Ponge, and D. Raabe, Materials Science and Engineering: A **527**, 7832 (2010).
[7] B. Gludovatz, A. Hohenwarter, D. Catoor, E. H. Chang, E. P. George, and R. O. Ritchie, Science **345**, 1153 (2014).
[8] S. Zhang, D. Sun, Y. Fu, and H. Du, Surf. Coat. Technol. **198**, 2 (2005).
[9] D. Holec, M. Friák, J. Neugebauer, and P. H. Mayrhofer, Phys. Rev. B Condens. Matter **85**, 064101 (2012).
[10] L. Zhou, D. Holec, and P. H. Mayrhofer, J. Appl. Phys. **113**, 043511 (2013).
[11] M. Shinn and S. A. Barnett, Appl. Phys. Lett. **64**, 61 (1994).
[12] H. C. Barshilia, A. Jain, and K. S. Rajam, Vacuum **72**, 241 (2003).
[13] P. C. Yashar and W. D. Sproul, Vacuum **55**, 179 (1999).
[14] B. N. Jaya, C. Kirchlechner, and G. Dehm, J. Mater. Res. **30**, 686 (2015).
[15] K. Matoy, H. Schönherr, T. Detzel, T. Schöberl, R. Pippan, C. Motz, and G. Dehm, Thin Solid Films **518**, 247 (2009).
[16] B. R. Lawn, A. G. Evans, and D. B. Marshall, J. Am. Ceram. Soc. **63**, 574 (1980).
[17] A. G. EVans and E. A. Charles, J. Am. Ceram. Soc. **59**, 371 (1976).
[18] X. Chu and S. A. Barnett, J. Appl. Phys. **77**, 4403 (1995).